PHYSICAL REVIEW B **108**, 245125 (2023)

Editors' Suggestion

Localized *f*-electron magnetism in the semimetal $Ce_3Bi_4Au_3$

M. O. Ajeesh,[1,*] S. K. Kushwaha,[2] S. M. Thomas,[1] J. D. Thompson,[1] M. K. Chan,[2] N. Harrison,[2]
J. M. Tomczak,[3,4] and P. F. S. Rosa[1]
[1]*Los Alamos National Laboratory, Los Alamos, New Mexico 87545, USA*
[2]*National High Magnetic Field Laboratory, Los Alamos, New Mexico 87545, USA*
[3]*Department of Physics, King's College London, Strand, London WC2R 2LS, United Kingdom*
[4]*Institute of Solid State Physics, TU Wien, Vienna 1040, Austria*

(Received 5 September 2023; revised 30 October 2023; accepted 20 November 2023; published 11 December 2023)

$Ce_3Bi_4Au_3$ crystallizes in the same noncentrosymmetric cubic structure as the prototypical Kondo insulator $Ce_3Bi_4Pt_3$. Here we report the physical properties of $Ce_3Bi_4Au_3$ single crystals using magnetization, thermodynamic, and electrical-transport measurements. Magnetic-susceptibility and heat-capacity data reveal antiferromagnetic order below $T_N = 3.2\,\text{K}$. The magnetic entropy S_{mag} reaches $R\ln 2$ slightly above T_N, which suggests localized $4f$ moments in a doublet ground state. Multiple field-induced magnetic transitions are observed at temperatures below T_N, which indicate a complex spin structure with competing interactions. $Ce_3Bi_4Au_3$ shows semimetallic behavior in electrical resistivity in contrast to the majority of reported cerium-based 343 compounds which are semiconducting. Electrical-resistivity measurements under hydrostatic pressure reveal a slight enhancement of T_N under pressures up to 2.3 GPa, which supports a scenario wherein $Ce_3Bi_4Au_3$ belongs to the far left of the Doniach phase diagram dominated by Ruderman-Kittel-Kasuya-Yosida interactions. Using realistic many-body simulations, we confirm the semimetallic electronic structure of $Ce_3Bi_4Au_3$ and quantitatively reproduce its local moment behavior in the paramagnetic state.

DOI: 10.1103/PhysRevB.108.245125

I. INTRODUCTION

Cerium-based ternary compounds crystallizing in the cubic $Ce_3X_4T_3$ (X denotes Bi and Sb and T is a transition metal) structure present a wide variety of ground-state properties owing to the delicate interplay between the crystal lattice, the electron filling, and the hybridization between f electrons and the conduction electron sea. For instance, the isoelectronic compounds $Ce_3Bi_4Pt_3$ and $Ce_3Sb_4Pt_3$ exhibit Kondo-insulating behavior in an intermediate valence regime [1–4], whereas the ground state of $Ce_3Bi_4Pd_3$ has been argued to be either a Weyl-Kondo semimetal or a Kondo insulator with a narrower gap compared to $Ce_3Bi_4Pt_3$ [5–10].

In contrast, substitution by group 11 transition metals, such as Cu or Au, tends to drive Ce ions into a localized 3+ state and tune the material towards a band insulating/semimetallic state [11–13]. Though $Ce_3Sb_4Au_3$ presents semiconducting behavior seemingly similar to that of the Pt counterpart, the origin of the gap cannot be Kondo hybridization. Instead, the electron count through the Zintl concept ($3Ce^{3+} + 4Sb^{3-} + 3Au^{1+} = +9 - 12 + 3$) is suggestive of a conventional semiconducting gap [14]. Interestingly, $Ce_3Sb_4Au_3$ shows a large specific heat coefficient at low temperatures, which is unexpected in a semiconductor with localized f electrons. This unusual behavior has been attributed to the presence of an f-level resonant state within a conventional band gap [15,16]. In the case of $Ce_3Sb_4Cu_3$, an activated behavior in the electrical resistivity with decreasing temperature was initially taken as evidence of a semiconducting gap [17]. Later studies using optical reflectivity and Hall measurements, however, argued against the presence of an energy gap, and the temperature dependence of the electrical resistivity was ascribed to changes in the carrier mobility, categorizing $Ce_3Sb_4Cu_3$ as a semimetal [13]. Finally, $Ce_3Sb_4Au_3$ does not order magnetically, whereas $Ce_3Sb_4Cu_3$ undergoes magnetic ordering at 10 K to a canted antiferromagnetic (AFM) phase [18–20].

$Ce_3Bi_4Au_3$, a less studied compound in the 343 family, also crystallizes in the cubic $Y_3Sb_4Au_3$-type structure (space group $I\bar{4}3d$) [14]. Magnetic susceptibility measurements reveal a Curie-Weiss behavior consistent with Ce^{3+} local moments which undergo antiferromagnetic ordering at $T_N = 2.9\,\text{K}$ [14]. Electrical-resistivity measurements in $R_3Bi_4Au_3$ (R = La, Nd, and Sm) revealed a weak decrease in resistivity on cooling with a corresponding residual resistivity ratio ($\rho_{300\,\text{K}}/\rho_{10\,\text{K}}$) of only about 1.3–1.4 [14]. This poor metallic behavior was taken as an indication that members of the $R_3Bi_4Au_3$ family are doped semiconductors with largely temperature-independent electrical resistivities. Notably, these materials show a large Seebeck value, which holds promise for thermoelectric applications [14,21,22].

In this article, we investigate the physical properties of $Ce_3Bi_4Au_3$ single crystals by means of magnetic, thermodynamic, and electrical-transport measurements. The magnetic ground state of $Ce_3Bi_4Au_3$ is characterized in detail along with the effect of magnetic field and hydrostatic pressure. Our results reveal localized f moments in a crystalline electric field doublet ground state. Under hydrostatic pressure, T_N

---

[*] ajeesh@lanl.gov

slowly increases, which indicates $Ce_3Bi_4Au_3$ is dominated by Ruderman-Kittel-Kasuya-Yosida (RKKY) interactions that lead to its AFM ground state. Many-body calculations, performed in the framework of density functional theory plus dynamical mean field theory (DFT + DMFT), reveal the presence of a small electron pocket at the Fermi level in the paramagnetic phase, which confirms its semimetallic nature. The simulations further yield a Curie-Weiss magnetic susceptibility in quantitative agreement with experiments. Together, our combined experimental and theoretical results enable a broader comparison between Ce 343 compounds and shed light on the distinct ground states in this family.

II. METHODS

Single crystals of $Ce_3Bi_4Au_3$ and $La_3Bi_4Au_3$ were grown by the Bi-flux method with a starting composition Ce(La):Au:Bi = 1:2:15. The starting materials were loaded into an alumina crucible and sealed in an evacuated quartz tube. The quartz tube was then heated to 850 °C at 85 °C/h and held at this temperature for 36 h, followed by a multistep cooldown to 750 °C in 1 h, then to 550 °C in 100 h, and finally to 400 °C in 50 h. Excess Bi flux was removed by centrifugation after heating the quartz tube to 450 °C. Single crystals of polyhedral shape with largest dimension of about 1.5 mm were obtained. The crystallographic structure was verified at room temperature by a Bruker D8 Venture single-crystal diffractometer equipped with Mo radiation.

Magnetization measurements were carried out in the temperature range 1.8–350 K and in magnetic fields to 7 T using a superconducting quantum interference device vibrating sample magnetometer (MPMS3, Quantum Design). High-field magnetization measurements to 30 T in pulsed magnetic fields were performed at the National High Magnetic Field Laboratory, Los Alamos, USA. The heat capacity was measured in a Quantum Design Physical Property Measurement System (PPMS) using a calorimeter that utilizes a quasiadiabatic thermal relaxation technique. Electrical-resistivity measurements were performed on polished crystals in a standard four-terminal method wherein electrical contacts to the samples were made using 12.5-μm platinum wires and silver paste. Magnetoresistance was obtained in the transverse geometry where the magnetic field was applied perpendicular to the current flow. Electrical-transport measurements under hydrostatic pressure were carried out using a double-layered piston-cylinder-type pressure cell with Daphne 7373 oil as the pressure-transmitting medium. The pressure inside the sample space was determined at low temperatures by the shift of the superconducting transition temperature of a piece of lead. Electrical resistivity was measured using an ac resistance bridge (Model 372, Lake Shore) at a measuring frequency of 13.7 Hz together with a PPMS. All measurements were performed on unoriented single-crystal samples.

For the many-body DFT + DMFT simulations, we initialized the crystal structure of $Ce_3Bi_4Au_3$ with atomic positions from Ref. [14] and the experimental lattice constant $a = 10.221$ Å of the present work. Within the confines of space group $I\bar{4}3d$, only the position (u, u, u) of the Bi site is not predetermined. We relax this coordinate within density functional theory (with the Perdew-Burke-Ernzerhof functional) using WIEN2K [23]. Dynamical mean field theory calculations were then performed in the same realistic setting (DFT + DMFT) as previously for $Ce_3Bi_4Pt_3$ [24,25] with the code of Haule *et al.* [26], which includes spin-orbit coupling, charge self-consistency, and full Coulomb interactions parametrized by a Hubbard $U = 5.5$ eV and Hund's $J = 0.68$ eV. The impurity problem was solved using continuous-time quantum Monte Carlo in the hybridization expansion and the Ce $4f$ hybridization was accounted for in an energy window of ±8 eV around the Fermi level. Results shown use the nominal double-counting scheme [26]. Magnetic degrees of freedom are assessed by sampling the local (impurity) spin susceptibility. Analytical continuation was performed as described in Ref. [26]. Transport properties were simulated in linear response, following the methodology of Ref. [27].

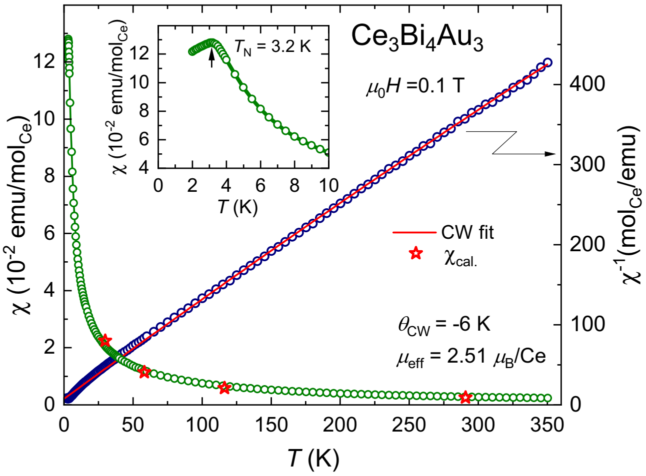

FIG. 1. Temperature dependence of the magnetic susceptibility $\chi = M/H$ (left axis) of $Ce_3Bi_4Au_3$ measured under magnetic field $\mu_0 H = 0.1$ T. The inverse magnetic susceptibility $\chi^{-1}(T)$ is plotted on the right axis. The red solid line is a fit using Curie-Weiss law in the temperature interval 100 K $\leqslant T \leqslant$ 350 K. The inset presents a close-up of the low-temperature $\chi(T)$ highlighting the peak at 3.2 K corresponding to the antiferromagnetic transition. The red star stands for the local susceptibility calculated from electronic structure simulations.

III. RESULTS AND DISCUSSION

A. Magnetic susceptibility and magnetization

The temperature-dependent magnetic susceptibility $\chi(T)$ of $Ce_3Bi_4Au_3$, measured in an applied magnetic field of $\mu_0 H = 0.1$ T, is depicted in Fig. 1. At high temperatures, $Ce_3Bi_4Au_3$ shows paramagnetic behavior, and its susceptibility follows the Curie-Weiss (CW) law. A CW fit to the $\chi^{-1}(T)$ data (Fig. 1, right axis) using $\chi(T) = \chi_0 + C/(T - \theta_W)$ in the temperature range 100 K $\leqslant T \leqslant$ 350 K yields $\chi_0 = 1.3(2) \times 10^{-4}$ emu/mol$_{Ce}$, the Curie constant $C = 0.79(1)$ emu K/mol$_{Ce}$, and the Weiss temperature $\theta_W = -6(1)$ K. The effective moment $\mu_{eff} = \sqrt{8C} = 2.51\mu_B$ is close to the expected value of $2.54\mu_B$ for a free Ce^{3+} ion. The negative value of θ_W indicates predominantly antiferromagnetic interaction between the moments. The deviation of $\chi(T)$ from

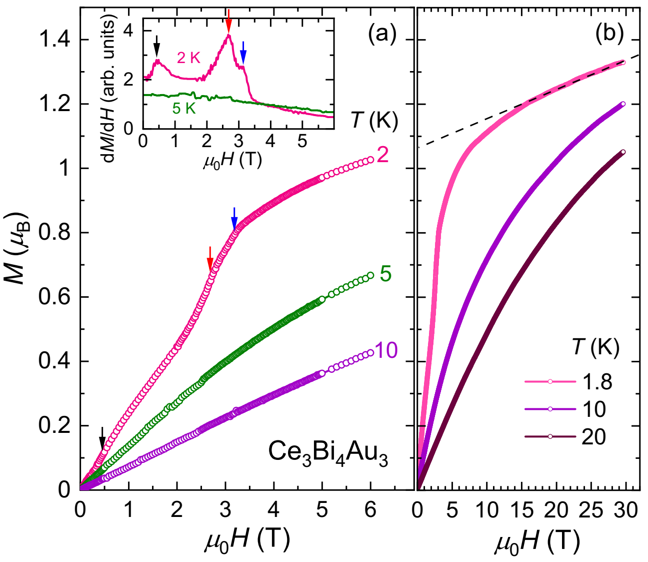

FIG. 2. (a) Magnetization of $Ce_3Bi_4Au_3$ versus applied magnetic field, measured at different temperatures. The derivative dM/dH is plotted in the inset. Various features in $M(H)$ are indicated by the arrows. (b) High-field magnetization measured at several temperatures.

CW behavior for temperatures below approximately 75 K is likely related to crystalline electric field effects as discussed below. At low temperatures, $Ce_3Bi_4Au_3$ orders antiferromagnetically at around $T_N = 3.2$ K, as evidenced by a cusplike feature in $\chi(T)$ (see the inset of Fig. 1). The magnetic transition temperature and the CW parameters are in good agreement with previously reported values [14].

The magnetization of $Ce_3Bi_4Au_3$ as a function of applied field $M(H)$ measured at different temperatures below and above T_N is plotted in Fig. 2. At $T = 2$ K, $M(H)$ displays several slope changes, which are likely associated with changes in the magnetic structure. Three noticeable features at $\mu_0H = 0.5$, 2.6, and 3.2 T (marked by arrows) are detected in derivative dM/dH curves plotted in the inset of Fig. 2(a). These multistep spin-reorientation transitions have been observed in other Ce-based materials and are a telltale sign of complex spin structures arising from competing exchange interactions (i.e., magnetic frustration) [28,29]. Figure 2(b) shows the isothermal magnetization for magnetic fields to 30 T. Here the magnetization data are scaled to match the low-field data from MPMS3 measurements. At $T = 1.8$ K, M reaches a value of $1.3\mu_B$/Ce at $\mu_0H = 30$ T, which is much smaller than the full saturation moment of the $J = 5/2$ multiplet. Similar magnetization values are also observed for isostructural compounds $Ce_3Sb_4Au_3$ [15,30–32] and $Ce_3Sb_4Cu_3$ [13,20] whose crystalline electric field (CEF) ground states are Kramers doublets.

B. Heat capacity

Figure 3(a) presents the temperature dependence of the heat capacity of $Ce_3Bi_4Au_3$ and, as a reference, the nonmagnetic isostructural compound $La_3Bi_4Au_3$, plotted as C_p/T versus log$T$. The sharp peak in C_p/T of $Ce_3Bi_4Au_3$ at $T = 3.2$ K corresponds to the AFM ordering and is consistent with the magnetic-susceptibility data. A weak feature in C_p/T below 2 K could be related to a change in the magnetic structure due to competing exchange interactions. In the inset of Fig. 3(a), the heat capacity of $Ce_3Bi_4Au_3$ in the temperature range 9–15 K is fitted with $C_p(T) = \gamma T + \beta T^3 + C_{\mathrm{Sch}}(T)$, where $C_{\mathrm{Sch}}(T)$ is the contribution from the excited CEF levels discussed below. The fit yields an estimate of the Sommerfeld coefficient $\gamma = 41(2)$ mJ/mol$_{\mathrm{Ce}}$K^2, which implies rather weak electron-correlation effects.

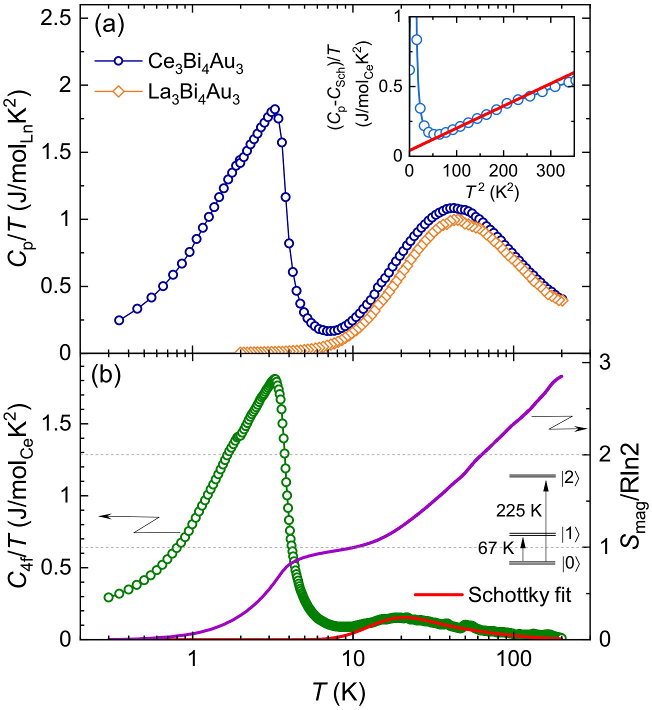

FIG. 3. (a) Temperature dependence of the heat capacity of $Ce_3Bi_4Au_3$ and the nonmagnetic isostructural compound $La_3Bi_4Au_3$, plotted as C_p/T versus log$T$. (b) Magnetic contribution to the heat capacity, plotted as $C_{4f}(T)/T$ versus T (left axis). Here C_{4f} is estimated by subtracting the heat capacity of the nonmagnetic reference compound $La_3Bi_4Au_3$ from that of $Ce_3Bi_4Au_3$. The red solid line is the calculated Schottky contribution assuming three doublet states. The calculated magnetic entropy $S_{\mathrm{mag}}(T)$ is displayed in units of $R\ln 2$ (right axis). The inset in (a) shows a fit to the heat capacity data, after subtracting the Schottky contribution, using $C_p(T) = \gamma T + \beta T^3$ in the temperature range 9–15 K.

The magnetic contribution to the heat capacity of $Ce_3Bi_4Au_3$ is estimated by subtracting the heat capacity of the nonmagnetic reference compound $La_3Bi_4Au_3$ [see Fig. 3(b)]. Here $C_p(T)$ of $La_3Bi_4Au_3$ is measured down to 2 K and the data are fitted with $C_p(T) = \gamma T + \beta T^3$ for 2–15 K to estimate $C_p(T)$ down to low temperatures. The magnetic entropy S_{mag}, obtained by integrating C_{4f}/T over T, reaches about 80% of $R\ln 2$ at T_N and presents a small plateau before continuously increasing with a further increase in temperature. This behavior corroborates a CEF doublet ground state which is well separated from the excited CEF levels. The large value of S_{mag} near T_N points to the localized nature of the Ce moments and a rather weak Kondo effect in $Ce_3Bi_4Au_3$. We note that the full magnetic entropy of $R\ln 2$ for a doublet state is recovered only at around 10 K, which can be ascribed to the formation of short-range correlations leading up to the AFM long-range order. Within the mean field approximation, the jump in heat capacity ΔC_{4f} at T_N can be used to estimate the Kondo scale [33,34]. Here $\Delta C_{4f} = 5.86$ J/mol$_{\rm Ce}$ K at T_N, yielding a Kondo temperature of $T_K \approx 4$ K. We note that this is probably an overestimation of T_K due to the broad nature of the heat capacity anomaly; however, this estimate also reflects the weak Kondo effect in $\rm Ce_3Bi_4Au_3$.

Further insights into the CEF scheme of $\rm Ce_3Bi_4Au_3$ can be obtained from $C_{4f}(T)$ data in the paramagnetic region, which reveals a broad hump centered around 20 K reminiscent of a Schottky anomaly associated with the excited CEF levels. Even though the overall crystal structure of $\rm Ce_3Bi_4Au_3$ has cubic symmetry, the Ce sites have tetragonal point symmetry due to the distorted tetrahedral arrangement of surrounding Au atoms. In the presence of a CEF with a tetragonal symmetry, the sixfold-degenerate levels of $\rm Ce^{3+}$ ion with total angular momentum $J = 5/2$ split into three Kramers doublets which are energetically separated from each other. Therefore, the high-temperature part of the $C_{4f}(T)$ data can be described by a Schottky contribution for a three-level system as

$$C_{\rm Sch}(T) = \frac{R}{T^2}\frac{\sum_i \sum_j g_i g_j \Delta_i(\Delta_i - \Delta_j)e^{-(\Delta_i+\Delta_j)/T}}{\left(\sum_i g_i e^{-\Delta_i/T}\right)^2}, \qquad (1)$$

where R is the gas constant; $i, j = 0, 1, 2$; g_i is the degeneracy of each level; and Δ_i is the energy separation from the ground state. Experimental data for $\rm Ce_3Bi_4Au_3$ in the temperature range 10–200 K are well reproduced by Eq. (1) with the first and second excited levels at 67 and 225 K, respectively. We note that $C_{4f}(T)$ become much smaller at higher temperatures and become comparable to the experimental error in the heat capacity of $\rm Ce_3Bi_4Au_3$ and $\rm La_3Bi_4Au_3$. Therefore, the highest excited CEF level is only a rough estimation. A schematic representation of the CEF levels is depicted in the inset of Fig. 3(b). A similar CEF scheme has also been reported for the isostructural compounds $\rm Ce_3Sb_4Au_3$ [15,30–32] and $\rm Ce_3Sb_4Cu_3$ [13,20].

The C_p/T of $\rm Ce_3Bi_4Au_3$ as a function of temperature for several applied magnetic fields is shown in Fig. 4. Initially, the peak in C_p/T shifts to lower temperatures with increasing field, a behavior typical of AFM ordering. For fields above 3 T, the peak in C_p/T becomes much broader and shifts to higher temperatures with a further increase in field. This is consistent with the field-induced spin reorientation observed in the magnetization data. The broad hump in C_p/T under higher fields corresponds to the crossover from the paramagnetic to the field-polarized phase.

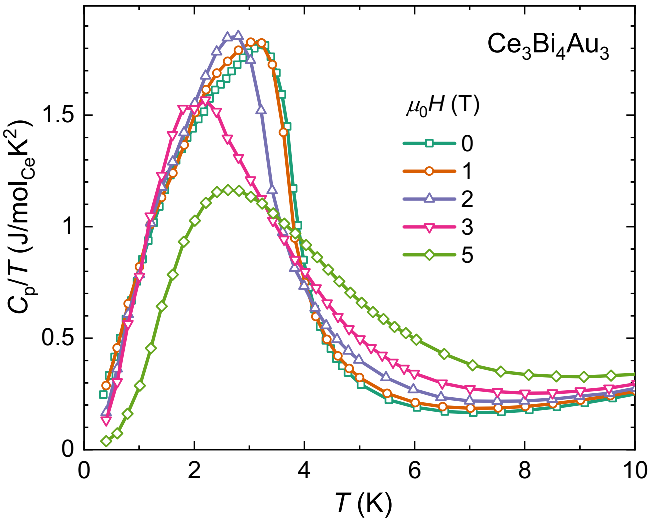

FIG. 4. Plot of C_p/T vs T of $\rm Ce_3Bi_4Au_3$ measured under different applied magnetic fields.

C. Electrical transport

The electrical resistivities $\rho(T)$ of $\rm Ce_3Bi_4Au_3$ and $\rm La_3Bi_4Au_3$ are shown in Fig. 5. Both materials exhibit semimetallic behavior with room temperature resistivities in the range of 1–3 mΩ cm. The $\rho(T)$ of both materials appear to be sample dependent, probably due to the presence of inclusions of unwanted phases due to excess flux used in the sample growth. For instance, the resistivity of polycrystalline $\rm La_3Bi_4Au_3$ reported earlier is an order of magnitude larger than that we obtained here [14]. The contributions from impurity inclusions in our crystals could not be removed even after carefully polishing the samples, which implies that the inclusions may be present within the bulk of the crystals. The effect of impurity inclusions on the magnetotransport data is discussed in Appendix A. Similar issues of impurity inclusions in electrical-transport data have been reported in other members of the 343 compounds [9,15].

The resistivity of $\rm Ce_3Bi_4Au_3$ presents a broad curvature centered around approximately 70 K, which is arguably attributed to additional scattering originating from thermal population of excited CEF levels. Note that the temperature

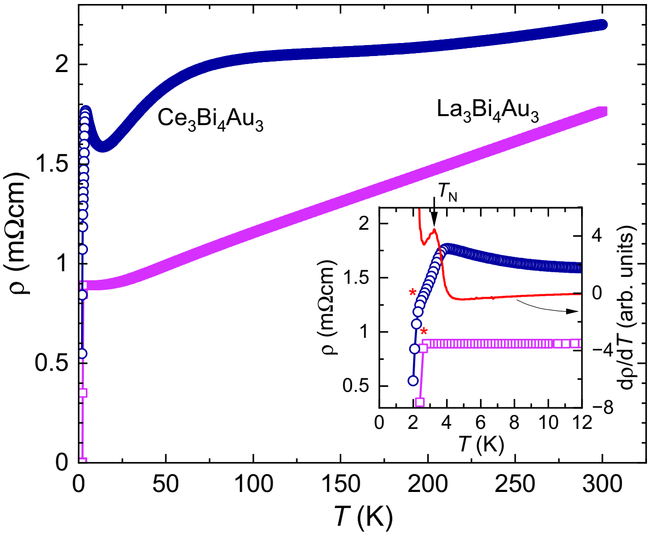

FIG. 5. (a) Temperature dependence of the electrical resistivity $\rho(T)$ of $\rm Ce_3Bi_4Au_3$ and $\rm La_3Bi_4Au_3$. The inset shows an enlarged view of the low-temperature part of $\rho(T)$. The temperature derivative of resistivity $d\rho/dT$ of $\rm Ce_3Bi_4Au_3$ is plotted on the right axis. Arrows indicate the anomalies corresponding to AFM ordering in $\rm Ce_3Bi_4Au_3$ and stars denote the superconducting transitions possibly coming from $\rm Au_2Bi$ inclusions.

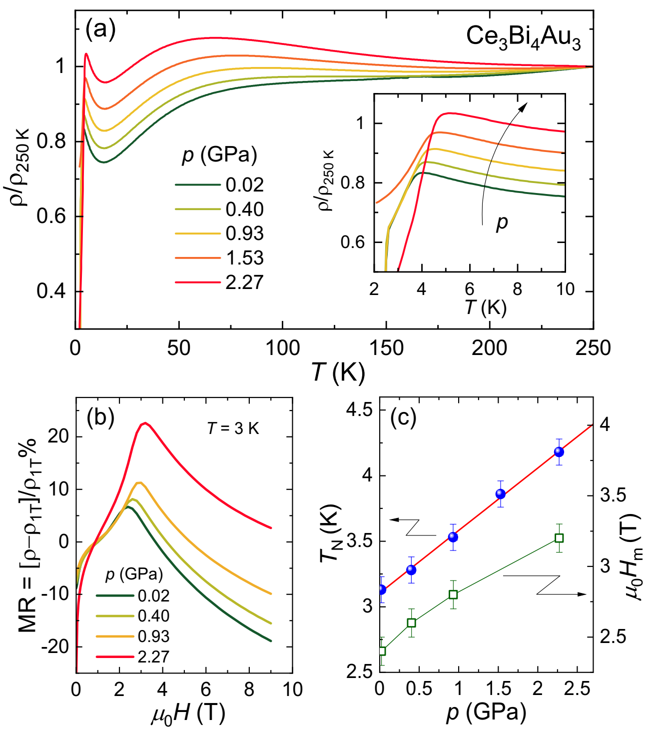

FIG. 6. (a) Normalized resistivity $\rho/\rho_{250\,\mathrm{K}}$ of $\mathrm{Ce_3Bi_4Au_3}$ vs T under several applied pressures. The inset shows an enlarged view of the low-temperature region of the curves. (b) Magnetoresistance $\mathrm{MR} = [\rho - \rho_{1\,\mathrm{T}}]/\rho_{1\,\mathrm{T}}$ as a function of magnetic field measured at $T = 3\,\mathrm{K}$ and different pressures. (c) Pressure dependence of the AFM transition temperature T_N (left axis) and the spin-reorientation critical field H_m (right axis). The red line is a linear fit to $T_N(p)$ data.

scale corresponding to the broad feature coincides with the CEF splitting obtained from heat-capacity data. At low temperatures, another increase in $\rho(T)$ is observed below 10 K followed by a pronounced kink at about 3.2 K due to the loss of spin-disorder scattering below T_N. The upturn in resistivity below 10 K coincides with the recovery of $R\ln 2$ entropy in heat capacity and likely corresponds to the onset of short-range interactions and/or Kondo scattering. Here T_N is determined from the maximum in the temperature derivative of resistivity $\mathrm{d}\rho/\mathrm{d}T$ (marked by the arrow in the inset of Fig. 5). The $\rho(T)$ of both $\mathrm{Ce_3Bi_4Au_3}$ and $\mathrm{La_3Bi_4Au_3}$ show a sudden drop below $T \approx 2.2\,\mathrm{K}$, which is likely due to the inclusion of superconducting Au-Bi binaries, such as $\mathrm{Au_2Bi}$ [35]. The lack of any associated feature in either magnetic susceptibility or heat capacity suggests that the impurity volume fraction is very small.

D. Effect of hydrostatic pressure

The evolution of the magnetic transition in $\mathrm{Ce_3Bi_4Au_3}$ is studied using electrical-transport measurements under hydrostatic pressure. The temperature dependence of the normalized electrical resistivity $\rho/\rho_{250\,\mathrm{K}}$ for several applied pressures is plotted in Fig. 6(a). The anomaly in resistivity corresponding to the AFM transition slightly shifts to higher temperatures with increasing pressure and reaches 4.6 K at $p = 2.27\,\mathrm{GPa}$ [see the inset of Fig. 6(a)]. The T_N, estimated from the maximum in the corresponding $\mathrm{d}\rho/\mathrm{d}T$ curve, as a function of pressure is plotted in Fig. 6(c). The T_N increases linearly with pressure and a linear fit to the data yields the slope $dT_N/dp = 0.48 \pm 0.01$ K/GPa. This enhancement in T_N is consistent with the Doniach phase diagram wherein the behavior of $T_N(p)$ is described by the competition between RKKY and Kondo interactions [36]. The strongly localized nature of the $4f$ moments and weak Kondo scale place $\mathrm{Ce_3Bi_4Au_3}$ in the far left of the Doniach phase diagram dominated by RKKY interaction. In this region, the increase in hybridization strength with pressure predominantly enhances the RKKY interaction and hence the magnetic order. Therefore, much higher pressure may be needed to suppress magnetism in $\mathrm{Ce_3Bi_4Au_3}$.

The relative change in transverse magnetoresistance $\mathrm{MR} = [\rho - \rho_{1\,\mathrm{T}}]/\rho_{1\,\mathrm{T}}$ as a function of magnetic field measured at $T = 3\,\mathrm{K}$ for several pressures is displayed in Fig. 6(b). Here $\mathrm{MR}(H)$ is obtained by symmetrizing the resistivity data measured in positive and negative magnetic fields to correct for the misalignment of electrical contacts. The $\mathrm{MR}(H)$ shows a steep increase for fields up to 1 T. This is possibly due to the presence of excess Bi or Au-Bi binaries in the samples. The fact that this feature persists up to temperatures much higher than T_N and also present in nonmagnetic $\mathrm{La_3Bi_4Au_3}$ (see Fig. 8 in Appendix A) supports an extrinsic origin. A detailed discussion of the effect of impurity inclusions on the magnetotransport is provided in Appendix A. It is also worth noting that very similar positive MR for fields up to 1 T is reported in flux grown samples of $\mathrm{(Ce, La)_3Bi_4Pt_3}$ [37]. A common feature in all these materials is the possibility of Bi-related inclusions in the samples. Nevertheless, the MR data above 1 T reflect the intrinsic properties of $\mathrm{Ce_3Bi_4Au_3}$, namely, positive MR followed by a sudden decrease at the spin-reorientation transition. The initial positive MR can be explained by the cyclotron motion of the conduction electrons [38]. The sudden decrease in MR at the spin-reorientation transition is due to the loss of spin-disorder scattering as the system goes from AFM to the field-polarized phase. The critical magnetic field for this transition monotonically increases with increasing pressure, as shown on the right axis of Fig. 6(c). This further substantiates that the AFM phase is stabilized by the application of pressures up to 2.3 GPa. Another noticeable feature in the pressure evolution of the $\rho(T)/\rho_{250\,\mathrm{K}}$ curves is that the broad hump in resistivity associated with the scattering from the excited CEF level gradually shifts to lower temperatures with increasing pressure. This would imply that the CEF scheme is modified by the application of pressure and the energy gap between the CEF ground state and the excited levels is slightly lowered by increasing pressure.

E. Electronic structure simulations

The $4f$ states of Ce hold the key to understanding the properties of $\mathrm{Ce_3Bi_4Au_3}$. Depending on the compound, $\mathrm{Ce_3}X_4T_3$, the physics can be very different: The $4f^0$ reference material $\mathrm{La_3Bi_4Au_3}$ is insulating within band theory [14] whereas $\mathrm{La_3Bi_4Pt_3}$ is metallic [4,39]. The extra $4f$ electron from cerium then leads, when neglecting electronic correlations, to a metallic band structure in $\mathrm{Ce_3Bi_4Au_3}$ (see Fig. 9 in

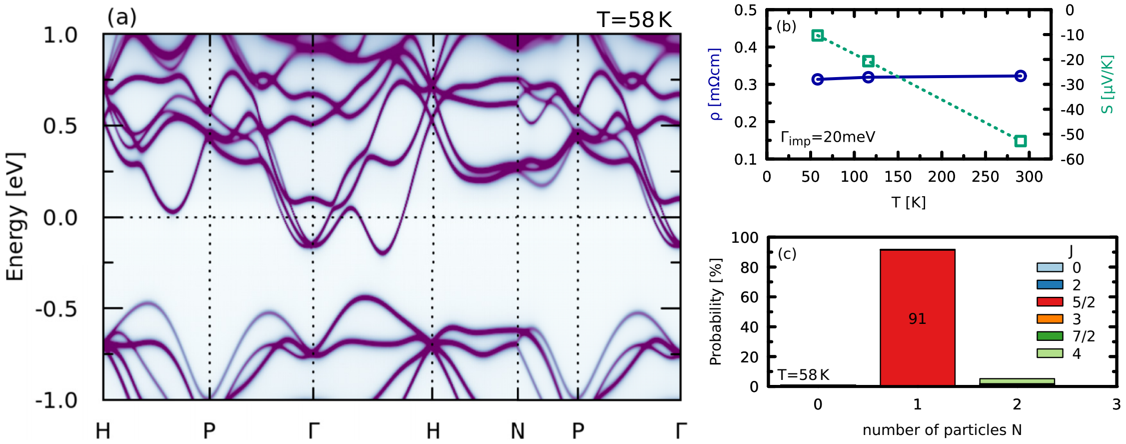

FIG. 7. (a) Simulated many-body spectral function of $Ce_3Bi_4Au_3$ along a selected high-symmetry path in the Brillouin zone. (b) Resistivity ρ (blue circles) and thermopower S (green squares) simulated as a function of temperature, with an added impurity scattering rate $\Gamma_{\text{imp}} = 20$ meV. (c) The valence histogram depicts the probability to find the $4f$ electrons of Ce in an atomic-limit state with occupation N and total angular momentum J. The data of (a) and (c) have been obtained at temperature $T = 58$ K.

Appendix B), whereas $Ce_3Bi_4Pt_3$ exhibits a semiconducting (hybridization) gap [4,40].

Appropriately treating many-body effects in the Kondo insulator $Ce_3Bi_4Pt_3$ results in a renormalization of the gap through an effective-mass enhancement of a factor of 10 as well as in the emergence of Ce $4f$ local moments above the lattice coherence temperature [4,25]. In contrast, the many-body spectral function of $Ce_3Bi_4Au_3$, displayed in Fig. 7(a) for $T = 58$ K, exhibits two electron pockets, one at the high-symmetry point Γ and a slightly deeper one between Γ and H, which corroborate the semimetallic behavior observed in experiments. Interestingly, in the Kondo insulator $Ce_3Bi_4Pt_3$, the global minimum of the conduction band occurs at the Γ point [25,41]. The difference between the spectra of $Ce_3Bi_4Au_3$ and $Ce_3Bi_4Pt_3$ thus goes beyond a mere shift of the chemical potential (to account for the additional electron per precious-metal atom). The energy of the two local minima (one at Γ and one between Γ and H) in the dispersion has been shown to be strongly influenced by the position (u, u, u) of the Bi site in the unit cell [24]: A larger u favors the band minimum to occur between Γ and H. Consistent with this observation, experiments (simulations) for $Ce_3Bi_4Au_3$ find $u = 0.08642$ ($u = 0.091$), which is larger than $u = 0.084$ [42] ($u = 0.088$) for $Ce_3Bi_4Pt_3$. In fact, already in the reference compound $La_3Bi_4Au_3$, band theory predicts the conduction-band minimum to be in between Γ and H (see Fig. 9). The band structure of $La_3Bi_4Au_3$ and the spectral function of $Ce_3Bi_4Au_3$ are comparable, with the crucial difference that in $Ce_3Bi_4Au_3$ the chemical potential has moved into the conduction band.

To understand this, we inspect the valence histogram in Fig. 7(c), which displays the decomposition of the Ce $4f$ electrons onto local states with well-defined occupation N and total angular momentum J: $Ce_3Bi_4Au_3$ is dominated by states with $N = 1$ and $J = 5/2$. We find valence fluctuations $\delta N = \sqrt{\langle (N - \langle N \rangle)^2 \rangle} = 0.29$ around the mean Ce $4f$ occupation $\langle N \rangle = 1.07$ in $Ce_3Bi_4Au_3$ at $T = 58$ K to be smaller than in the Kondo insulator $Ce_3Bi_4Pt_3$ (where $\delta N = 0.36$ with $\langle N \rangle = 1.02$ [25]). Still, the presence of valence fluctuations indicates that the $4f$ electrons are not fully localized. Their participation in the bonding means that there is more itinerant charge available than in the $4f^0$ reference $La_3Bi_4Au_3$. As a consequence, the chemical potential has to move up into the conduction band.

The instantaneous local moment of $Ce_3Bi_4Au_3$, $\mu_{\text{inst}} = g_J\sqrt{\langle J^2 \rangle}\mu_B/\hbar = g_J\sqrt{\langle j(j+1) \rangle}\mu_B \approx 2.65\mu_B$ (using $g_{J=5/2} = 0.857$), is comparable to both the local moment of isolated Ce^{3+} ions (mentioned above) and simulations of $Ce_3Bi_4Pt_3$ ($\mu_{\text{inst}} = 2.64\mu_B$ [25]). However, the standard deviation $\delta J = 0.56$ of the total angular momentum is substantially smaller than $\delta J = 0.81$ of $Ce_3Bi_4Pt_3$, again confirming the experimentally inferred stronger localization of the f states in $Ce_3Bi_4Au_3$. Finally, contrary to $Ce_3Bi_4Pt_3$ and $Ce_3Bi_4Pd_3$, the instantaneous local moment in $Ce_3Bi_4Au_3$ is hardly screened over time, resulting (when averaged over time) in a Curie-Weiss-like local magnetic susceptibility $\chi_{\text{loc}}(\omega = 0)$ that is in excellent agreement with the experimental uniform susceptibility $\chi(q = 0, \omega = 0)$ (see Fig. 1).

Based on the (DMFT) electronic structure, we simulate transport properties [see Fig. 7(b)]. The resistivity is only weakly temperature dependent, consistent with experiment and the semimetallic spectrum. Note that the calculations use an added temperature-independent scattering rate $\Gamma_{\text{imp}} = 20$ meV to mimic sources of finite lifetimes other than electronic correlations, e.g., impurity scattering. The amplitude Γ_{imp} is small compared to the scattering from electron-electron correlations: At the Fermi level, the Ce $4f$ self-energy evaluates to $|\text{Im}\Sigma(\omega = 0)| = 109$ meV (184 meV) at $T = 58$ K ($T = 290$ K) when averaged over the $J = 5/2$ states. However, in $Ce_3Bi_4Au_3$, transport is mostly driven by the (non-$4f$) conduction electrons and the decay of their current is dominated by the impurity scattering [see Fig. 10(a) in Appendix C]. On an absolute scale, the simulated resistivity is too small by almost an order of magnitude compared to the experimental values. This discrepancy could point to larger effects of disorder, e.g., structural defects or the impurity inclusions discussed above. Indeed, the resistivity of $Ce_3Sb_4Cu_3$ was shown to vary by a factor of 10, depending on the sample preparation [43]. Similar effects could be responsible for the semimetallic behavior in the experimental resistivity of $La_3Bi_4Au_3$ in contrast to the DFT predicted insulating gap. Alternatively, off-stoichiometry could cause a shrinking of the electron pockets, leading to a larger resistivity.

Further insight comes from the Seebeck coefficient S. As the ratio of two response functions [44], S is largely insensitive to the magnitude of scattering in metals[1] [see Fig. 10(a)]. Its sign provides information on the dominant type of charge carriers. Congruent with the presence of electron pockets in Fig. 7(a), the simulated Seebeck coefficient in Fig. 7(b) is negative. Future measurement of S can thus serve as a validation of the simulated electronic structure. If the thermopower of $Ce_3Bi_4Au_3$ turns out to be positive in experiments, as it is for $Ce_3Sb_4Au_3$ [43] and $Ce_3Sb_4Cu_3$ [47], this might point towards extrinsic influences or electronic structure effects not captured here.

IV. SUMMARY

We have investigated the physical properties of cubic $Ce_3Bi_4Au_3$ by magnetic, thermodynamic, and electrical-transport measurements on single-crystalline samples. Magnetization and heat-capacity data revealed that the $4f$ moments in $Ce_3Bi_4Au_3$ are dominantly localized and order antiferromagnetically below $T_N = 3.2$ K. The localized nature of the Ce moments and weak/negligible Kondo interactions were further evidenced by the slight enhancement of T_N under the application of hydrostatic pressure. The electrical resistivity of $Ce_3Bi_4Au_3$ showed semimetallic behavior on cooling, which was corroborated by realistic many-body calculations that reveal the presence of small electron pockets below the Fermi level. In addition, the simulations quantitatively reproduced the local moment behavior in the paramagnetic state. Our combined experimental and theoretical investigations showed that the additional electron per formula unit from Au atom compared to the Pt/Pd counterparts render $Ce_3Bi_4Au_3$ as a $4f$-localized semimetallic member of the highly tunable $Ce_3X_4T_3$ family of compounds.

Upon publication, the simulation data will be available from [48].

ACKNOWLEDGMENTS

We acknowledge constructive discussions with M. M. Bordelon. The conception of this work as well the crystal synthesis was supported by the U.S. Department of Energy, Office of Basic Energy Sciences "Science of 100 T" program. J.M.T. acknowledges support from the Austrian Science Fund (FWF) through project BandITT Grant No. P 33571. Calculations were performed on the Vienna Scientific Cluster. M.O.A. acknowledges funding from the Laboratory Directed Research & Development Program. Measurements under pressure were supported by the U.S. Department of Energy, Office of Basic Energy Sciences "Quantum Fluctuations in Narrow Band Systems" program. Scanning electron microscope and energy dispersive x-ray measurements were performed at the Center for Integrated Nanotechnologies, an Office of Science User Facility operated for the U.S. Department of Energy Office of Science. The National High Magnetic Field Laboratory-Pulsed-Field Facility is funded by the National Science Foundation Cooperative Agreement No. DMR-1644779, the State of Florida, and the U.S. Department of Energy. M.K.C. acknowledges support from NSF IR/D program while serving at the National Science Foundation. Any opinion, findings, and conclusions or recommendations expressed in this material are those of the author(s) and do not necessarily reflect the views of the National Science Foundation.

APPENDIX A: MAGNETOTRANSPORT: EFFECT OF IMPURITY INCLUSIONS

The transverse magnetoresistance $\mathrm{MR} = [\rho - \rho_{0\mathrm{T}}]/\rho_{0\mathrm{T}}$ as a function of magnetic field measured at different temperatures for $Ce_3Bi_4Au_3$ and $La_3Bi_4Au_3$ is shown in Fig. 8. The MR(H) of both compounds show very similar behavior apart from the contributions from the magnetic transitions in $Ce_3Bi_4Au_3$. The sharp increase in MR for fields up to 1 T is clearly seen in both compounds and is nearly temperature independent up to 50 K. In addition, the increase in MR also shows strong sample dependence for both compounds. All these results point to an extrinsic origin for the behavior, possibly due to the presence of Bi or Au-Bi inclusions in the samples. The resistivity data on all samples show superconducting transitions at low temperatures coming from tiny inclusions of Au-Bi binaries. These inclusions may be present in the form of irregular filaments that would give rise to current inhomogeneities. In addition, the inclusions could range from elemental bismuth to Bi-Au binary

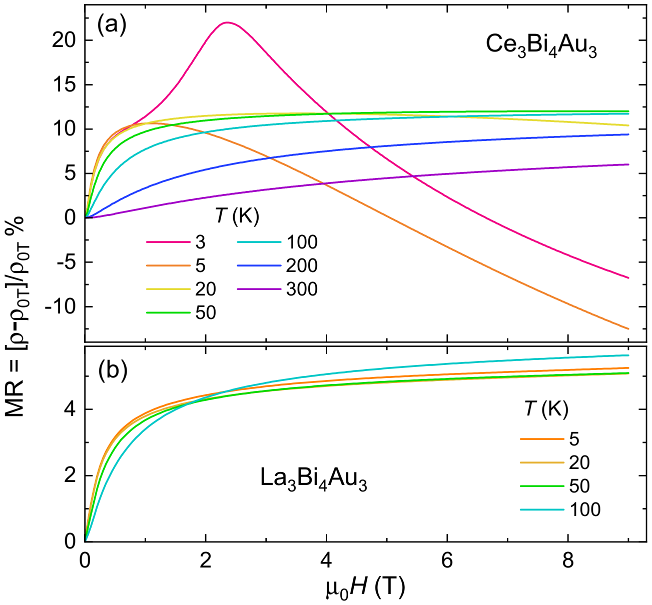

FIG. 8. Transverse magnetoresistance $\mathrm{MR} = [\rho - \rho_0]/\rho_0$ as a function of magnetic field measured at different temperatures for (a) $Ce_3Bi_4Au_3$ and (b) $La_3Bi_4Au_3$.

---

[1] See, however, Refs. [45,46].

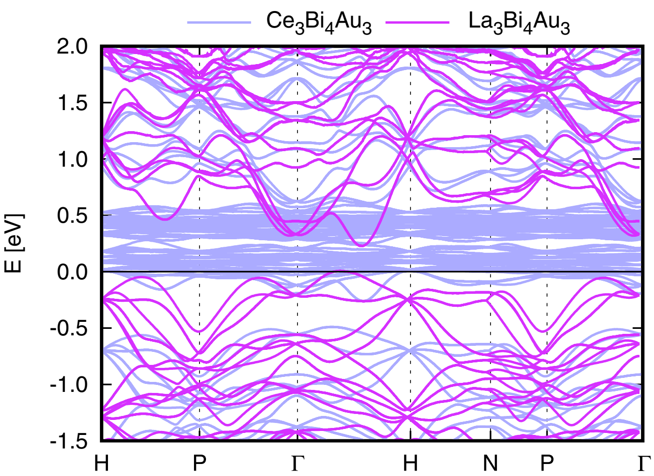

FIG. 9. Band structures of $Ce_3Bi_4Au_3$ (light blue) and $La_3Bi_4Au_3$ (magenta) (see Ref. [14]) within DFT. The system is insulating (metallic) in the absence (presence) of the $4f$ electron, in direct opposition to the related pair of materials $R_3Bi_4Pt_3$ (R = Ce and La) [4].

compounds of varying stoichiometry. The normal state of such binaries often has semimetallic behavior with strong magnetoresistance properties. In the case of elemental Bi, strongly anisotropic magnetotransport behavior is observed along with a semimetal to insulatorlike behavior change under magnetic field applied along the trigonal axis of the Bi single crystal [49]. Effects can be further complicated as the inclusions can have geometries such as a thin layer or filament shape, which could lead to different properties compared to bulk samples [50–52]. Notably, a very similar behavior in MR for fields up to 1 T was reported in flux grown samples of (Ce, La)$_3Bi_4Pt_3$ [37]. Even though the authors used a multiband model to explain the MR data, the striking similarity to the MR of (Ce, La)$_3Bi_4Au_3$ with a significantly different electronic band structure (induced by the additional electron per formula unit from Au compared to Pt) is rather suspicious. A more plausible explanation is the effect of semimetallic inclusions common to all these materials.

APPENDIX B: DENSITY FUNCTIONAL THEORY

In Fig. 9 we compare the band structures of $La_3Bi_4Au_3$ (insulating, magenta) and $Ce_3Bi_4Au_3$ (metallic, blueish). The spectral function of $Ce_3Bi_4Au_3$ in Fig. 7(a) incorporates many-body effects within DMFT and is shown for the same path in the Brillouin zone. As the Ce $4f$ states are mostly localized, the many-body spectrum of $Ce_3Bi_4Au_3$ is reminiscent of the $La_3Bi_4Au_3$ band-structure, albeit with a chemical potential that is shifted into the conduction band owing to finite hybridization with the $4f$ states.

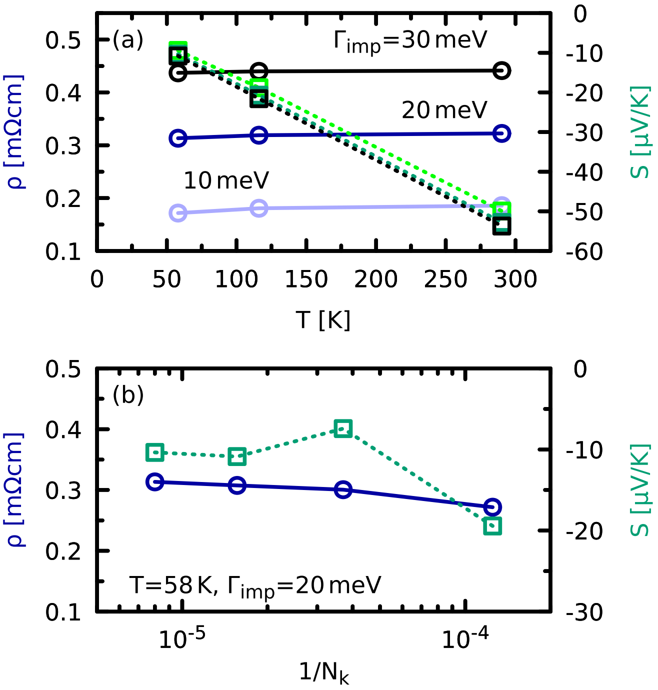

FIG. 10. Simulated resistivity and Seebeck coefficient. (a) Dependence on the added impurity scattering rate (light to dark: $\Gamma_{imp} = 10, 20, 30$ meV): blue, resistivity ρ; green, Seebeck coefficient S. (b) Convergence of ρ and S with the Brillouin zone discretization (N_k denotes the number of reducible **k** points). The calculations in Fig. 7(b) use the finest mesh ($N_k = 50^3$).

APPENDIX C: TRANSPORT SIMULATIONS

As alluded to in the main text, the Seebeck coefficient S of metals is virtually insensitive to (reasonable) changes in the scattering rate Γ [see Fig. 10(a)]. The resistivity ρ of metals is instead basically proportional to Γ. In the case of $Ce_3Bi_4Au_3$, it is Γ_{imp} that dominates the response of the conduction electrons. Transport simulations of (semi)metals are delicate. In Fig. 10(b) we therefore assess the convergence of the response with respect to the Brillouin zone discretization. At the lowest temperature considered here, $T = 58$ K, and for $\Gamma_{imp} = 20$ meV, both ρ and S appear reasonably converged for a momentum grid with 50^3 reducible points.

---

[1] M. F. Hundley, P. C. Canfield, J. D. Thompson, Z. Fisk, and J. M. Lawrence, Hybridization gap in $Ce_3Bi_4Pt_3$, Phys. Rev. B **42**, 6842(R) (1990).

[2] Z. Fisk, J. L. Sarrao, J. D. Thompson, D. Mandrus, M. F. Hundley, A. Miglori, B. Bucher, Z. Schlesinger, G. Aeppli, E. Bucher, J. F. DiTusa, C. S. Oglesby, H.-R. Ott, P. C. Canfield, and S. E. Brown, Kondo insulators, Physica B **206–207**, 798 (1995).

[3] P. S. Riseborough, Heavy fermion semiconductors, Adv. Phys. **49**, 257 (2000).

[4] J. M. Tomczak, Thermoelectricity in correlated narrow-gap semiconductors, J. Phys.: Condens. Matter **30**, 183001 (2018).

[5] S. Dzsaber, L. Prochaska, A. Sidorenko, G. Eguchi, R. Svagera, M. Waas, A. Prokofiev, Q. Si, and S. Paschen, Kondo insulator to semimetal transformation tuned by spin-orbit coupling, Phys. Rev. Lett. **118**, 246601 (2017).

[6] H.-H. Lai, S. E. Grefe, S. Paschen, and Q. Si, Weyl-Kondo semimetal in heavy-fermion systems, Proc. Natl. Acad. Sci. USA **115**, 93 (2018).

[7] S. Dzsaber, X. Yan, M. Taupin, G. Eguchi, A. Prokofiev, T. Shiroka, P. Blaha, O. Rubel, S. E. Grefe, H.-H. Lai, Q. Si, and S. Paschen, Giant spontaneous Hall effect in a nonmagnetic Weyl–Kondo semimetal, Proc. Natl. Acad. Sci. USA **118**, e2013386118 (2021).

[8] S. K. Kushwaha, M. K. Chan, J. Park, S. M. Thomas, E. D. Bauer, J. D. Thompson, F. Ronning, P. F. S. Rosa, and N. Harrison, Magnetic field-tuned Fermi liquid in a Kondo insulator, Nat. Commun. **10**, 5487 (2019).

[9] M. O. Ajeesh, S. M. Thomas, S. K. Kushwaha, E. D. Bauer, F. Ronning, J. D. Thompson, N. Harrison, and P. F. S. Rosa, Ground state of $Ce_3Bi_4Pd_3$ unraveled by hydrostatic pressure, Phys. Rev. B **106**, L161105 (2022).

[10] J. M. Tomczak, Isoelectronic tuning of heavy fermion systems: Proposal to synthesize $Ce_3Sb_4Pd_3$, Phys. Rev. B **101**, 035116 (2020).

[11] K. Katoh and M. Kasaya, Magnetic and transport properties of $Ce_3Au_{3-x}Pt_xSb_4$, J. Phys. Soc. Jpn. **65**, 3654 (1996).

[12] C. D. W. Jones, K. A. Regan, and F. J. DiSalvo, $Ce_3Cu_xPt_{3-x}Sb_4$: Modifying the properties of a Kondo insulator by substitutional doping, Phys. Rev. B **60**, 5282 (1999).

[13] P. Wachter, L. Degiorgi, G. Wetzel, and H. Schwer, $Ce_3Cu_3Sb_4$: A semimetal with a spontaneous magnetic moment, Phys. Rev. B **60**, 9518 (1999).

[14] E. M. Seibel, W. Xie, Q. D. Gibson, and R. J. Cava, Synthesis, structure, and basic magnetic and thermoelectric properties of the light lanthanide aurobismuthides, Inorg. Chem. **55**, 3583 (2016).

[15] H.-O. Lee, Y.-J. Jo, L. Balicas, P. Schlottmann, C. L. Condron, V. A. Sidorov, P. Klavins, S. M. Kauzlarich, J. D. Thompson, and Z. Fisk, Unique *f*-level resonant state within the gap in $Ce_3Au_3Sb_4$ single crystals: Magnetic, thermal, and transport properties, Phys. Rev. B **76**, 155204 (2007).

[16] H.-O. Lee, V. A. Sidorov, P. Schlottmann, C. Condron, P. Klavins, S. M. Kauzlarich, J. D. Thompson, and Z. Fisk, Localized states within the gap of $Ce_3Au_3Sb_4$, Physica B **403**, 1476 (2008).

[17] S. Patil, Z. Hossain, P. L. Paulose, R. Nagarajan, L. C. Gupta, and C. Godart, $Ce_3Cu_3Sb_4$: The first Ce-based semiconducting ferromagnet, Solid State Commun. **99**, 419 (1996).

[18] P. Wachter, L. Degiorgi, G. Wetzel, H. Schwer, K. Mattenberger, T. Herrmannsdorfer, and P. Fischer, $Ce_3Cu_3Sb_4$: A canted antiferromagnetic semimetal, Acta Phys. Pol. A **97**, 43 (2000).

[19] T. Herrmannsdörfer, P. Fischer, P. Wachter, G. Wetzel, and K. Mattenberger, Neutron diffraction investigation of magnetic ordering in $Ce_3Cu_3Sb_4$, Solid State Commun. **112**, 135 (1999).

[20] W. Schnelle and R. K. Kremer, Thermodynamic properties and magnetism of $Ce_3Cu_3Sb_4$, J. Phys.: Condens. Matter **13**, 6387 (2001).

[21] P. Witas, J. Goraus, M. Fijałkowski, and A. Ślebarski, Thermoelectric and magnetic properties of $Ce_3Cu_{3-x}Au_xSb_4$ compounds, J. Appl. Phys. **129**, 125110 (2021).

[22] D. Young, K. Mastronardi, P. Khalifah, C.-C. Wang, R. J. Cava, and A. P. Ramirez, $Ln_3Au_3Sb_4$: Thermoelectrics with low thermal conductivity, Appl. Phys. Lett. **74**, 3999 (1999).

[23] P. Blaha, K. Schwarz, F. Tran, R. Laskowski, G. K. H. Madsen, and L. D. Marks, WIEN2k: An APW+lo program for calculating the properties of solids, J. Chem. Phys. **152**, 074101 (2020).

[24] M. Pickem, E. Maggio, and J. M. Tomczak, Resistivity saturation in Kondo insulators, Commun. Phys. **4**, 226 (2021).

[25] J. M. Tomczak, Realistic many-body theory of Kondo insulators: Renormalizations and fluctuations in $Ce_3Bi_4Pt_3$, arXiv:1904.01346.

[26] K. Haule, C.-H. Yee, and K. Kim, Dynamical mean-field theory within the full-potential methods: Electronic structure of $CeIrIn_5$, $CeCoIn_5$, and $CeRhIn_5$, Phys. Rev. B **81**, 195107 (2010).

[27] J. M. Tomczak, K. Haule, and G. Kotliar, Signatures of electronic correlations in iron silicide, Proc. Natl. Acad. Sci. USA **109**, 3243 (2012).

[28] J. von Boehm and P. Bak, Devil's stairs and the commensurate-commensurate transitions in CeSb, Phys. Rev. Lett. **42**, 122 (1979).

[29] S. M. Thomas, P. F. S. Rosa, S. B. Lee, S. A. Parameswaran, Z. Fisk, and J. Xia, Hall effect anomaly and low-temperature metamagnetism in the Kondo compound $CeAgBi_2$, Phys. Rev. B **93**, 075149 (2016).

[30] M. Kasaya, K. Katoh, M. Kohgi, T. Osakabe, and N. Sato, Valence change and physical properties in semiconducting mixed-valent rare-earth compounds, Physica B **199–200**, 534 (1994).

[31] D. T. Adroja, B. D. Rainford, Z. Hossain, E. A. Goremychkin, R. Nagarajan, L. C. Gupta, and C. Godart, Magnetism and crystal field of $Ce_3Au_3Sb_4$, Physica B **206–207**, 216 (1995).

[32] S.-H. Baek, H. Sakai, H. Lee, Z. Fisk, E. D. Bauer, and J. D. Thompson, Crystal-electric-field effects and quadrupole fluctuations in $Ce_3Au_3Sb_4$ detected by Sb NQR, Phys. Rev. B **82**, 035203 (2010).

[33] C. D. Bredl, F. Steglich, and K. D. Schotte, Specific heat of concentrated Kondo systems: (La, Ce)Al_2 and $CeAl_2$, Z. Phys. B **29**, 327 (1978).

[34] J. A. Blanco, M. de Podesta, J. I. Espeso, J. C. Gómez Sal, C. Lester, K. A. McEwen, N. Patrikios, and J. Rodríguez Fernández, Specific heat of $CeNi_xPt_{1-x}$ pseudobinary compounds and related dilute alloys, Phys. Rev. B **49**, 15126 (1994).

[35] B. W. Roberts, Survey of superconductive materials and critical evaluation of selected properties, J. Phys. Chem. Ref. Data **5**, 581 (1976).

[36] S. Doniach, The Kondo lattice and weak antiferromagnetism, Physica B **91**, 231 (1977).

[37] M. Hundley, A. Lacerda, P. Canfield, J. Thompson, and Z. Fisk, Magnetoresistance of the Kondo insulator $Ce_3Bi_4Pt_3$, Physica B **186–188**, 425 (1993).

[38] H. Yamada and S. Takada, Magnetoresistance due to electron-spin scattering in antiferromagnetic metals at low temperatures, Prog. Theor. Phys. **49**, 1401 (1973).

[39] L. Li, G.-X. Zhi, Q. Zhu, C. Wu, Z. Yang, J. Du, J. Yang, B. Chen, H. Wang, C. Cao, and M. Fang, Superconductivity in the nodal-line compound $La_3Pt_3Bi_4$, Phys. Rev. Res. **4**, L032004 (2022).

[40] K. Takegahara, H. Harima, Y. Kaneta, and A. Yanase, Electronic band structures of $Ce_3Pt_3Sb_4$ and $Ce_3Pt_3Bi_4$, J. Phys. Soc. Jpn. **62**, 2103 (1993).

[41] C. Cao, G.-X. Zhi, and J.-X. Zhu, From trivial Kondo insulator $Ce_3Pt_3Bi_4$ to topological nodal-line semimetal $Ce_3Pd_3Bi_4$, Phys. Rev. Lett. **124**, 166403 (2020).

[42] A. Severing, J. D. Thompson, P. C. Canfield, Z. Fisk, and P. Riseborough, Gap in the magnetic excitation spectrum of $Ce_3Bi_4Pt_3$, Phys. Rev. B **44**, 6832 (1991).

[43] P. Witas, J. Goraus, P. Zajdel, K. Balin, J. Koperski, J. Lelatko, and A. Ślebarski, Impact of microstructure on the thermoelectric properties of the ternary compound $Ce_3Cu_3Sb_4$, Mater. Charact. **123**, 256 (2017).

[44] K. Behnia, *Fundamentals of Thermoelectricity* (Oxford University Press, Oxford, 2015).

[45] P. Sun, B. Wei, J. Zhang, J. M. Tomczak, A. M. Strydom, M. Søndergaard, B. B. Iversen, and F. Steglich, Large Seebeck effect by charge-mobility engineering, Nat. Commun. **6**, 7475 (2015).

[46] F. Garmroudi, M. Parzer, A. Riss, C. Bourgès, S. Khmelevskyi, T. Mori, E. Bauer, and A. Pustogow, High thermoelectric performance in metallic NiAu alloys via interband scattering, Sci. Adv. **9**, eadj1611 (2023).

[47] K. Fess, W. Kaefer, C. Thurner, K. Friemelt, C. Kloc, and E. Bucher, Magnetic and thermoelectric properties of $R_3Cu_3Sb_4$ ($R =$ La, Ce, Gd, Er), J. Appl. Phys. **83**, 2568 (1998).

[48] https://doi.org/10.5281/zenodo.8298875.

[49] X. Du, S.-W. Tsai, D. L. Maslov, and A. F. Hebard, Metal-insulator-like behavior in semimetallic bismuth and graphite, Phys. Rev. Lett. **94**, 166601 (2005).

[50] H. T. Chu, P. N. Henriksen, J. Jing, H. Wang, and X. Xu, Magnetic-field dependence of Hall resistance in thin films of pure bismuth, Phys. Rev. B **45**, 11233 (1992).

[51] H. T. Chu, P. N. Henriksen, and J. Alexander, Resistivity and transverse magnetoresistance in ultrathin films of pure bismuth, Phys. Rev. B **37**, 3900 (1988).

[52] M. Lu, R. J. Zieve, A. van Hulst, H. M. Jaeger, T. F. Rosenbaum, and S. Radelaar, Low-temperature electrical-transport properties of single-crystal bismuth films under pressure, Phys. Rev. B **53**, 1609 (1996).